

**The Role of Solar Flares in the Variability of the Extreme Ultraviolet  
Solar Spectral Irradiance**

by

**Rachel Allison Hock**

A.B., Wellesley College, 2006

M.S., University of Colorado, 2008

A thesis submitted to the  
Faculty of the Graduate School of the  
University of Colorado in partial fulfillment  
of the requirements for the degree of  
Doctor of Philosophy  
School of Arts and Sciences

2012

UMI Number: 3508124

All rights reserved

INFORMATION TO ALL USERS

The quality of this reproduction is dependent on the quality of the copy submitted.

In the unlikely event that the author did not send a complete manuscript and there are missing pages, these will be noted. Also, if material had to be removed, a note will indicate the deletion.



UMI 3508124

Copyright 2012 by ProQuest LLC.

All rights reserved. This edition of the work is protected against unauthorized copying under Title 17, United States Code.



ProQuest LLC.  
789 East Eisenhower Parkway  
P.O. Box 1346  
Ann Arbor, MI 48106 - 1346

## Chapter 4

### EVE Flare Catalog

Flares have traditionally been classified based on their physical extent and brightness in  $H\alpha$  ( $H\alpha$  importance) and the peak soft X-ray flux from 0.1 to 0.8 nm as recorded by the GOES satellites (GOES class). Using EVE observations of flares, we have discovered that flares with the same magnitude and similar profiles in the GOES soft X-ray 0.1 – 0.8 nm (SXR) can have radically different EUV responses. Figure 4.1 shows light curves for five M1.0 flares. While each flare has the same peak GOES SXR flux, the light curves in EUV emissions are different. There are not only differences in the strength of the EUV response but also in the timing of the flare peaks in the EUV. The size of flare in  $H\alpha$  and brightness in the soft X-rays are not sufficient to describe the EUV irradiance changes. The high temporal cadence and continuous observing mode of SDO allow for the first time the statistical study of solar flares in the EUV. The EVE flare catalog developed out of the need to quantify and organize the new observations of solar flares from EVE. This chapter describes the creation of the EVE flare catalog and what information is contained in it.

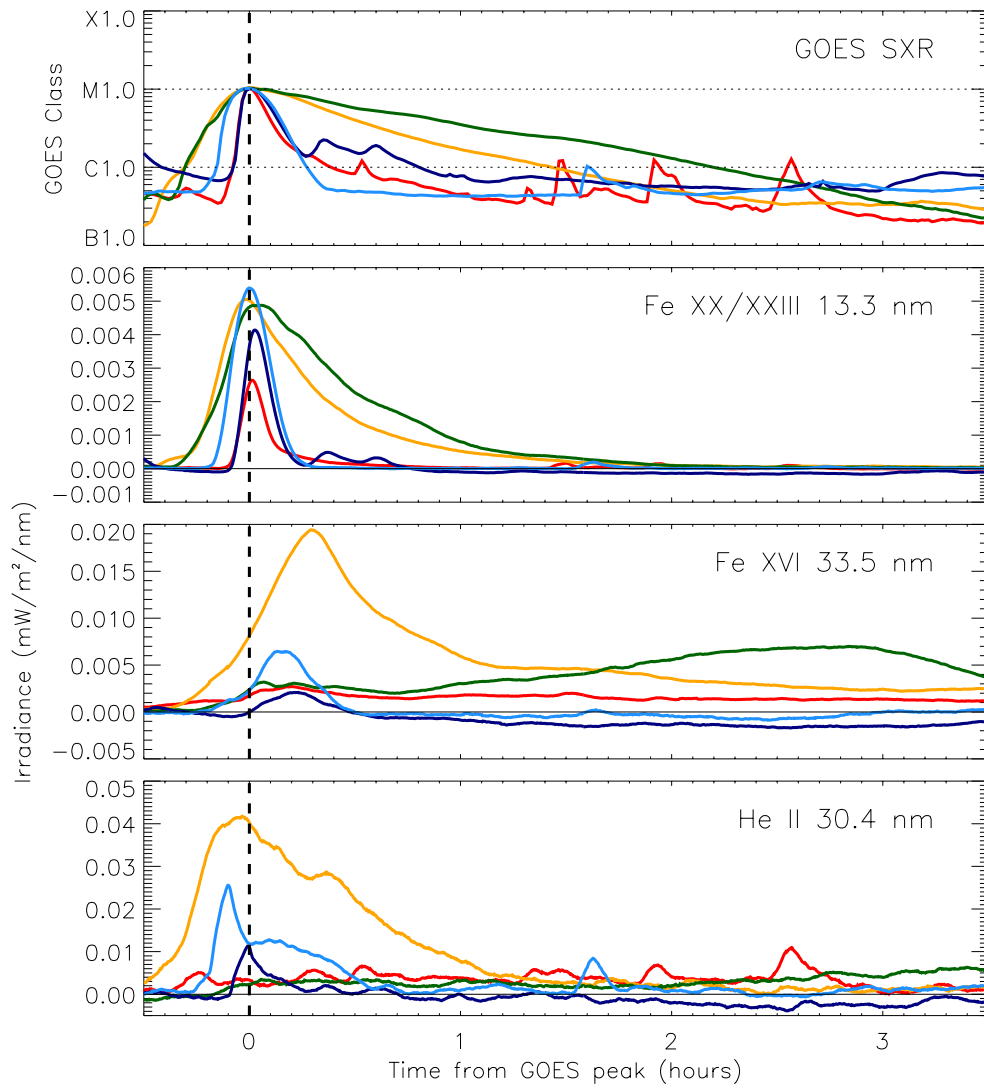


Figure 4.1: EUV light curves for five different M1.0 flares. The top panel shows the GOES SXR light curves, shifted temporally so the peaks occur at 0 hours. The next three panels show a hot coronal line (10 MK), warm coronal line (2.7 MK) and a cool transition region line (50,000 K) respectively. Notice not only the differences in strength of the EUV lines but also the differences in timing of the EUV peaks between the five flares.

## 4.1 Development of the EVE Flare Catalog

The EVE flare catalog was developed to gather information about each flare from multiple sources and to create tools to understand the origin and evolution of the event. The catalog itself is a collection of IDL structures, graphs, images, and movies. The IDL structures form a database containing vital information for quantitative study of flares while the graphs, images, and movies allow for the visualization of the SDO data for each flare. The EVE flare catalog uses a variety of data sources to provide a comprehensive study of solar flares.

These data sources come from several different providers and give a more complete picture than what is possible using data only from EVE. NOAA's Space Weather Prediction Center (SWPC, <http://www.swpc.noaa.gov/>) issues several daily reports summarizing solar events and provides soft X-ray irradiances from GOES in the 0.05–0.4 nm range and the 0.1–0.8 nm range with 1-minute cadence. RHESSI (Lin et al. 2002) measures the hard X-ray component of solar flares, which is useful for studying the impulsive phase of a flare. Images from SDO AIA (Lemen et al. 2012) provide spatially-resolved information about the flare's morphology. In addition to EUV irradiance measured by MEGS, flare location is determined using two other channels on EVE: ESP and SAM. Another source of the flare location comes from the Heliophysics Event Knowledgebase (HEK, Hurlburt et al. 2012), which combines automated data mining using feature-detection methods and high-performance visualization systems for data markup.

### 4.1.1 Seeding the Flare Catalog

The EVE flare catalog is built off of the daily flare list issued in NOAA's Solar and Geophysical Activity Summary (SGAS) reports, which uses data from GOES. Presently, there are small gaps in GOES coverage when the spacecraft goes into eclipse. Eclipse periods occur twice a year for 45 to 60 days with outages from a few minutes to just over an hour. This results in a loss of GOES coverage about 1% of the time. SDO also has biennial eclipse seasons. The GOES and SDO eclipse seasons are at the same time of the year but generally do not overlap. As a result, there are flares that are not captured by GOES that SDO observes and some GOES flares have no SDO observations.

I defined a threshold to include only flares with GOES class C1.0 or larger. While EVE observes flares smaller than C1.0, these flares may only be seen in the hottest flare lines such as Fe XX/XXIII at 13.3 nm. Flares smaller than C1.0 are also generally spatially small, making it harder to observe their topology in EUV images.

Seeding the catalog from the GOES flare list with flares C1.0 or larger allows the EVE flare catalog to meet three important criteria. (1) Results obtained with the catalog are compatible with the current definitions and classifications of solar flares. (2) The catalog is comprehensive so that as many events as possible can be studied. (3) Finally, only events that are above EVE's noise threshold are included.

Using this definition of events for the EVE flare catalog, I am able to examine over 750 flares from 1 May 2010 to 31 August 2011. In order to uniquely identify each flare in the catalog, I devised a flare ID which includes the date and peak time as recorded by GOES as well as the GOES class. The flare ID is a string containing the year, day of year (DOY), calendar date, peak time, and GOES class. For example, a M5.0 flare that occurred on 21 July 2001 (DOY 202) at 04:56 UT would have a flare ID of 2001202\_21JUL\_0456\_M5.0. The day of year is useful for sorting chronologically and because EVE data are stored in files containing the day of year. The calendar data is included for ease of the user and because the other SDO instrument teams (HMI and AIA) store their data by the year, month, and day. The peak time and GOES class serves a unique identifier.

#### **4.1.2 Structure of the EVE Flare Catalog**

The EVE flare catalog is modular. Table 4.1 gives a brief overview of each module. After the catalog is seeded, each module can be run independently for either one flare, a group of flares, or all flares. There are two advantages to this. First, it is easy to rerun parts of the catalog if, for example, there is a new version of EVE data. Second, this allows for future expansion without rewriting the majority of the code. An undergraduate over summer 2011 wrote IDL code to analyze the coronal dimmings associated with CMEs. By writing a wrapper around her code, it is possible to add the analysis of coronal dimmings to the EVE flare catalog without changing any of already-existing code. Some modules are dependent on the output of another module. Most rely on the GOES and Pre-flare module which, in part, defines the start, peak, and

end times of the flare.

The computer code that is used to generate the EVE flare catalog is written in IDL (Version 7.1.1) and utilizes some routines from SolarSoft, a set of integrated software libraries, data bases, and system utilities which provide a common programming and data analysis environment for solar physics (Freeland & Handy 1998). The majority of the EVE flare catalog code is automated. Human input, however, is currently necessary for several things and is supplied through a IDL widget, which also allows for user comments to added. Throughout the EVE flare catalog, times are saved both as a string with the day, month, year and time in UT and as the modified Julian date. The former is easily human readable while the later is easier to use within IDL. The details of the code, the IDL structures, and the user widget will be discussed in the following sections as each module is introduced.

Table 4.1: EVE flare catalog modules with their data sources, outputs, and a brief description.

Section	Module	Data Source(s)	Output	Description
4.2	GOES and Pre-flare	NOAA reports, GOES SXR	GOES IDL structure, PRE_FLARE IDL structure	Extract information from the NOAA SGAS reports; calculate parameters associated with the Neupert effect; determine time interval for pre-flare irradiance calculations.
4.3	NOAA Events	NOAA reports	NOAA_EVENTS IDL structure	Find any flare-associated radio bursts, H $\alpha$ flares, or other solar events from the NOAA Events reports.
4.4	Active Region	NOAA reports	AR IDL structure	Extract information about the active region associated with the flare from the NOAA SRS reports.
4.5	Flare Location	EVE, NOAA reports, HEK	LOCATION IDL structure	Calculate the location on the solar disk of the flare.
4.6	CME	Various CME catalogs	CME IDL structure	Determine flare-CME association.
4.7	EVE	EVE, RHESSEI, GOES SXR	EVL IDL structure, Quicklook PDF, EVL PDF	Extract pre-flare and peak irradiance, flare energy, and rise time and duration of the flare for each line, diode, and band in the EVE Level 2 EVL data product. Generate various graphs of GOES, EVE, and RHESSEI light curves during the flare.
4.8	AIA-EVE Movie	EVE, AIA, GOES SXR	AIA-EVE MPEG	Generate a MPEG movie of AIA images and EVE light curves.
4.9	Comments	User	FLAGS IDL structure	User supplied comments via an IDL widget.

## 4.2 GOES and Pre-flare Module

After seeding the catalog, the GOES and Pre-flare module is run to generate two IDL structures: `GOES` and `PRE_FLARE`. The `GOES` structure (Table 4.2) contains basic information about the X-ray flare. The flare start, peak, and end times as well as the GOES class, location, and Active Region number are extracted from the daily NOAA SGAS reports. The other parameters are calculated from both the GOES SXR and the GOES short channel light curves.

Table 4.2: Description of the `GOES` IDL structure

Tag Name	Type	Description
<code>flare_id</code>	String	Flare ID
<code>date</code>	String	String containing the date of the flare
<code>year</code>	Integer	Year of the flare
<code>doy</code>	Integer	Day of year of the flare
<code>start_time</code>	String	Start time of the flare (UT)
<code>start_time_jd</code>	Double	Julian date of the start time of the flare
<code>peak_time</code>	String	Peak time of the flare (UT)
<code>peak_time_jd</code>	Double	Julian date of the start time of the flare
<code>end_time</code>	String	End time of the flare (UT)
<code>end_time_jd</code>	Double	Julian date of the end time of the flare
<code>peak_class</code>	String	GOES flare class
<code>peak_flux</code>	Float	Flux equivalent of GOES flare class
<code>bkgd_class</code>	String	Background level of the GOES SXR flux
<code>bkgd_flux</code>	Float	Flux equivalent of GOES background class
<code>peak_flux_short</code>	Float	Peak irradiance in the GOES short channel
<code>bkgd_flux_short</code>	Float	Background irradiance in the GOES short channel
<code>peak_time_short</code>	String	Peak time of the flare (UT) in the GOES short channel
<code>peak_time_short_jd</code>	Double	Julian date of the start time of the flare in the GOES short channel
<code>neupert_peak</code>	Float	Maximum in the time derivative of the GOES SXR flux during the rising phase of the flare
<code>neupert_peak_time</code>	String	Neupert peak time
<code>neupert_peak_time_jd</code>	Double	Julian date of the Neupert peak time
<code>location</code>	String	Location of flare from GOES flare report (if given)
<code>longitude</code>	Integer	Longitude of flare (if given)
<code>latitude</code>	Integer	Latitude of flare (if given)
<code>ar_id</code>	Integer	NOAA active region number associated with flare (if any).

The Neupert peak is important for studying the impulsive phase. As discussed in Section 3.4.1, the Neupert effect is an empirical relationship between the time-derivation of the SXR and the HXR. Here, we take the time derivative of the GOES SXR flux and look for the maximum during the rise of the flare (flare

start to peak). The time and value of the maximum are saved as the Neupert peak time and value. This provides an estimate of when the impulsive phase is expected to peak in RHESSI HXR and EVE He II 30.4 nm light curves.

The GOES SXR light curves are also used to determine a time period to use to calculate the pre-flare irradiance, stored in the `PREFLARE` structure (Table 4.3). When we use EVE data to study flares, it is important to subtract the pre-flare irradiance. Irradiance measures the energy coming from the entire solar disk. Flares, however, are localized events. By subtracting the pre-flare irradiance, we are able to isolate only the flare contribution to the irradiance. For lines and bands that increase by orders of magnitude during a flare like the GOES SXR, the pre-flare irradiance does not contribute significantly to the irradiance at the peak of a flare. The majority of EUV lines, however, increase by less than a factor of 2 and the pre-flare irradiance makes up a large portion of the irradiance at the peak of a flare. The pre-flare irradiance also varies a great deal between flares.

Table 4.3: Description of the `PRE_FLARE` IDL structure

Tag Name	Type	Description
<code>flare_id</code>	String	Flare ID
<code>start_time</code>	String	Start time of the pre-flare period (UT)
<code>start_time_jd</code>	Double	Julian date of the start time of the pre-flare period
<code>end_time</code>	String	End time of the pre-flare period (UT)
<code>end_time_jd</code>	Double	Julian date of the end time of the pre-flare period

The issue becomes what is the “correct” pre-flare irradiance. In this flare catalog, we use the same pre-flare time interval for all the EUV lines and bands. The pre-flare module defines that interval using the GOES SXR flux. The pre-flare time is a 4-minute window centered on the minimum in the GOES SXR flux prior to the flare. This minimum is found by looking from the flare start time back to the previous flare or 45 minutes, whichever is closer to the flare start time. Figure 4.2 shows several examples of how the pre-flare window is defined.

This pre-flare window is used to calculate the background GOES class for the flare. The background

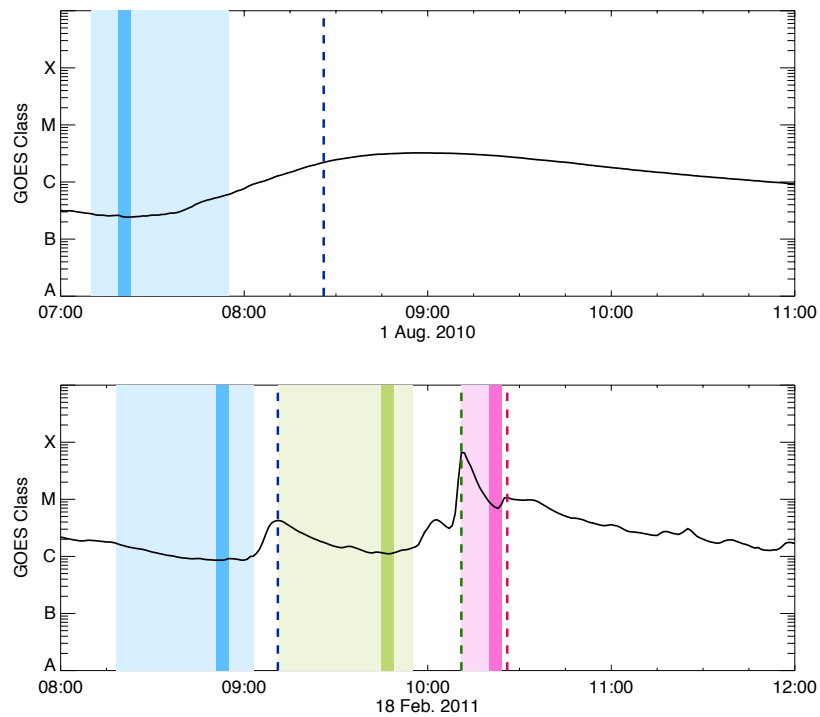


Figure 4.2: Several examples of how the pre-flare window is determined. For each flare, the light shaded region is the time range used for finding the pre-flare minimum in the GOES SXR. The dark shaded region is the 4-minute window used calculating the pre-flare irradiances. The vertical dashed line show the peak of each flare.

irradiance,  $E_{bkgd}$  is the average of 4-minute window around the minimum time:

$$E_{bkgd} = \langle E(t_{min} - 2 \text{ minutes} : t_{min} + 2 \text{ minutes}) \rangle \quad (4.1)$$

A C9.0 flare that occurs with a background of B5.0 is a stronger flare than a C9.0 flare with a background of C8.0. This background level will become more important as solar activity picks up and more flares happen during the decay phase of a prior flare.

### 4.3 NOAA Events Module

In addition to reporting solar flares from GOES, NOAA tracks other solar events that are recorded in the daily NOAA Solar Events reports. These events provide a greater context for the solar flare and provide a way to differentiate flares and possibly EUV irradiance changes. A subset of these events, called the “energetic events”, is available in SGAS report which is used to seed the catalog.

The NOAA Solar Events report is a compilation of individual reports of solar events such as X-ray flares, radio bursts, etc. Each event is assigned an arbitrary event number which groups several reports into a single event. The NOAA Events module searched through all the events for the day of the flare and finds the event which includes the X-ray flare by matching by the date, peak time, and GOES class from the GOES IDL structure. The module then find all other entries in the report with that event number and saves in them in the NOAA\_EVENTS IDL structure (Table 4.4) based on the type of report. Most of the substructures in NOAA\_EVENTS are empty as not all types of solar events are routinely reported or associated with solar flares. For example, the presence of a filament is a static event while solar flares are transient so NOAA will not associate a filament with the flare. The useful events included optical or H $\alpha$  flares (`fla_struct`) and sweep frequency radio bursts (`rsp_struct`).

For solar flares with H $\alpha$  signatures, NOAA reports both the optical importance and the location of the flare. The H $\alpha$  importance denotes the area in square degrees of heliocentric latitude that the flare occupies on the disk in H $\alpha$ . The importances range from S for subflares to 4 for the largest flares (Table 4.5) It is often appended with the qualitative brightness qualifier: F (faint), N (normal), or B (brilliant).

Many of the flares in the EVE flare catalog do not have corresponding optical flares. There are two

Table 4.4: Description of the NOAA\_EVENTS IDL structure

Tag Name	Type	Description
flare_id	String	Flare ID
event_id	String	Event number assigned by NOAA
bsl_struct	Structure	“Bright surge on limb” report
dsf_struct	Structure	“Filament disappearance” report
epl_struct	Structure	“Eruptive prominence on limb” report
fil_struct	Structure	“Filament” report
fla_struct	Structure	“Optical flare observed in H $\alpha$ ” report
for_struct	Structure	“Forbush decrease” (decrease in cosmic rays) report
gle_struct	Structure	“Ground-level event” report
lps_struct	Structure	“Loop prominence system” report
pca_struct	Structure	“Polar cap absorption” report
rbr_struct	Structure	“Fixed-frequency radio burst” report
rns_struct	Structure	“Radio noise storm” report
rsp_struct	Structure	“Sweep frequency radio burst” report
spy_struct	Structure	“Spray” report
xfl_struct	Structure	“SXI X-ray flare from GOES Solar X-ray Imager” report
xra_struct	Structure	“X-ray event from SWPC’s Primary or Secondary GOES spacecraft” report
flags	Byte array	Set if each type of report occurred
notes	String	Additional notes

Table 4.5: Relationship between H $\alpha$  importance and flare area corrected for foreshortening. A square degree at the center of the solar disk is roughly 12 Mm on a side or at 1 AU, 17 arc-seconds.

H $\alpha$ importance	Flare area (sq. deg.)
S	< 2.0
1	2.1 – 5.1
2	5.2 – 12.4
3	12.5 – 24.7
4	> 24.7

reasons this may happen. First, the flare may not be visible in H $\alpha$ . Some of the flares observed by EVE are small both in magnitude and in spatial extent as the Sun is currently in the rising phase of the solar cycle. H $\alpha$  locations are determined by eye from ground-based observations so small brightenings associated with smaller flares may be hard to detect. Second, there is no H $\alpha$  location if there are no H $\alpha$  observations during the flare. H $\alpha$  is a ground-based measurement. Observations can only be made during the day when the Sun is visible and the weather cooperates. These effects are partially negated by using a network of H $\alpha$  telescopes across the globe. Currently, however, H $\alpha$  observations are intermittent so the H $\alpha$  location is

not available for many of the EVE flares.

NOAA also reports sweep frequency solar radio bursts. There are several types of sweep frequency radio bursts, which are summarized in Table 4.6 and Figure 4.3, that are associated with solar flares. Table 4.7 shows where in the solar atmosphere different radio wavelengths are formed. There is a general trend that shorter radio wavelengths originate deeper in the atmosphere.

Table 4.6: Types of solar radio bursts.

Type	Solar Origin	Observational Signature
Type I	Solar noise storms. Not associated with solar flares.	Many short, narrow-band bursts in the meter wavelength range.
Type II	Formed by coronal shock waves. Associated with Moreton waves observed in H $\alpha$ or EIT waves observed in EUV wavelengths as well as CMEs.	Emission strips with narrow bandwidths and drift slowly from high to low frequencies.
Type III	Formed by electrons traveling along open field lines during hard X-ray (HXR) precursors to solar flares.	“Normal” bursts: when the electrons travel outward. “Reverse slope” (RS) bursts: when the electrons are traveling downward. “Bidirectional” bursts: two electron beams (one traveling upward, one downward).
Type IV	Occur with some major flare events; they begin 10 to 20 minutes after flare maximum and can last for hours. Attributed to synchrotron emission from energetic electrons trapped in magnetic clouds that travel into space (Lang 2009).	Appear as a smooth continuum of broadband bursts primarily in the meter wavelength range.
Type V	The gradual phase companion to Type III bursts	In the dekameter range.
Type VI		Series of Type III bursts over a period of 10 minutes or more with no period longer than 30 minutes without activity.
Type VII		Series of Type III and Type V bursts over a period of 10 minutes or more with no period longer than 30 minutes without activity.
CTM	Continuum storm	Long-lasting solar radio noise storm, in which the intensity varies smoothly with frequency over a wide range in the meter and decimeter wavelengths.

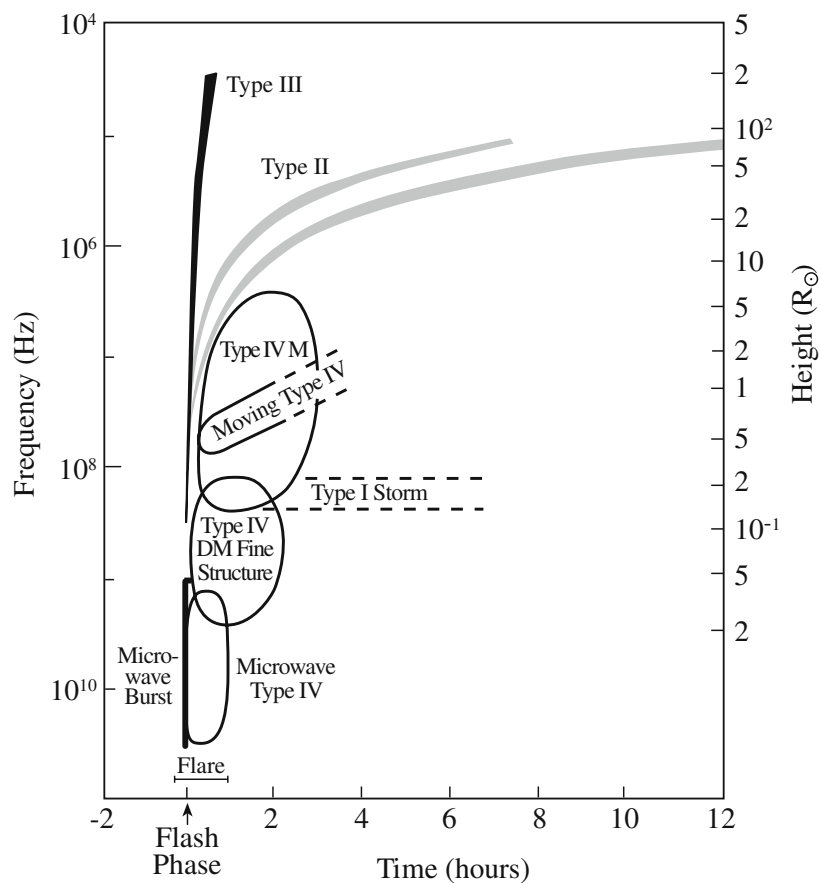


Figure 4.3: Schematic representation of radio bursts associated with major solar flares. Solar flares are associated with several different types of radio emission, depending on the frequency (left vertical axis) and time after the flare (bottom axis). Here, the impulsive phase of the flare is indicated at 0 hours. Dynamic spectra at frequencies of about  $10^8$  Hz show bursts that drift from high to low frequencies as time goes on. The different drift rates depend on the type of burst: Type II radio bursts are attributed to shock waves exciting plasma oscillations while Type II originate from electron beams. The height scale (right vertical axis) corresponds to the height, in units of the Sun's radius, at which the coronal electron density yields a plasma frequency corresponding to the frequency on the left-hand side. From Lang (2009).

Table 4.7: Solar radio spectrum (Source: NOAA)

Level of origin	Frequency (MHz)	Wavelength
Lower Chromosphere	15400	1.9 cm
	8800	3.4 cm
Middle Chromosphere	4995	6.0 cm
	2695	11.1 cm
Upper Chromosphere	1415	21.2 cm
	610	49.2 cm
	410	73.2 cm
Lower Corona	245	1.2 m
Upper Corona	75 – 25	4.0 – 12.0 m

#### 4.4 Active Region Module

The last type of report from NOAA is the daily Solar Region Summary (SRS) report containing information about the location, size, and complexity of each active region visible on the solar disk. The active region module extracts the information contained in the SRS reports for the active region associated with the flare and stores it in the AR IDL structure (Table 4.8).

Table 4.8: Description of the AR IDL structure

Tag Name	Type	Description
<code>flare_id</code>	String	Flare ID
<code>date</code>	String	Date of the active region report
<code>year</code>	Integer	Year of the active region report
<code>doy</code>	Integer	Day of year of the active region report
<code>ar_id</code>	Integer	Active region number associated with flare
<code>location</code>	String	Location of active region
<code>longitude</code>	Integer	Longitude of active region
<code>latitude</code>	Integer	Latitude of active region
<code>area</code>	Float	Area of active region corrected for projection effects in fraction of a hemisphere
<code>mcintosh_class</code>	String	McIntosh class
<code>mwso_magnetic_class</code>	String	Mt. Wilson magnetic class
<code>longitude_extent</code>	Integer	Longitudinal extent of active region in degrees
<code>sunspot_number</code>	Integer	Number of sunspots associated with active region

The vast majority of solar flares originate in active regions. Understanding whether differences in active regions are correlated with differences in the EUV signature of flares to is important as active region properties are currently used in predicting whether a region will flare.

While some of the information in the SRS reports such as active region area, longitudinal extend, and number of sunspots, are straightforward, the two classification schemes (the McIntosh classification system and the Mt. Wilson magnetic classification system) are somewhat subjective and have complicated definitions. The McIntosh system (McIntosh 1990) is an updated form of the Zurich classification (Kiepenheuer 1953) and uses white light data. In the McIntosh system each group is given three letters. The first letter known as the Z-value is the modified Zurich class and is a general description of the complexity (unipolar or bipolar) and size of the region. The second letter is the p-value and describes the penumbra of the largest spot. The final letter known as the c-value describes the sunspot distribution for bipolar regions. The definitions of each letter are given in Table 4.9.

The Mt. Wilson magnetic classification is based on almost 100 years of observations at the Mt. Wilson Solar Observatory and describes the magnetic complexity of a sunspot group. It has three main classes: unipolar ( $\alpha$ ), bipolar ( $\beta$ ), and complex ( $\gamma$ ). Unipolar groups are either single sunspots or groups of sunspot where all the spots have the same polarity. Bipolar groups contain at least two spots of opposite polarity. Often a bipolar group is made of more than two spots where the preceding spots have one polarity while the following have the opposite. In a  $\beta$ -class group, there is a clear division between polarities. The  $\gamma$  class contains complex groups of both polarities that are so irregularly disturbed that they can not be classified as bipolar. A hybrid class exists,  $\beta\gamma$ , where the group is bipolar but there is not distinct north-south division between polarities.

Table 4.9: McIntosh classification of sunspots

Z-values	Modified Zurich classification
	Unipolar sunspot.
A	The spot does not have a penumbra. No length restrictions.
	Bipolar sunspot group.
B	No spots have penumbrae. No length restrictions.
	Bipolar sunspot group.
C	One spot has a penumbra. No length restrictions.
	Bipolar sunspot group.
D	Both leading and following spots have penumbrae. Group is less than $10^\circ$ in length.
	Bipolar sunspot group.
E	Both leading and following spots have penumbrae. Group is between $10^\circ$ and $15^\circ$ in length.
	Bipolar sunspot group.
F	Both leading and following spots have penumbrae. Group is greater than $15^\circ$ in length.
	Unipolar sunspot.
H	The spot has a penumbra. No length restrictions.
p-values	Penumbra of largest spot
x	No penumbra
r	Rudimentary penumbra
s	Small and symmetric penumbra
a	Small and asymmetric penumbra
h	Large and symmetric penumbra
k	Large and asymmetric penumbra
c-values	Sunspot distribution
x	Undefined (for unipolar sunspots)
o	Open
i	Intermediate with no inter spots having mature penumbrae.
c	Compact with at least one inner spot having a mature penumbra.

#### 4.5 Location Module: Determining the Location of a Solar Flare

The location of a solar flare on the disk of the Sun is important for several reasons. Overall, the corona experiences limb brightening. Active regions on the limb appear brighter than active regions at disk center. However, for flares, the reverse seems to be true. There is a smaller increase in EUV irradiance from flares at the limb versus flares at disk center (Chamberlin et al. 2008). Furthermore, flares at the limb may be partially occulted: their footpoints could be behind the limb and not contributing to the irradiance signature. While this thesis will not focus on how to account for these location effects, they are nevertheless important to remember when comparing flares. Second, in order to compare the EUV irradiance signature of solar flares with the topology observed in EUV images, we need to know where to look in the images. This is particularly important when there are multiple active regions on the solar disk. Finally, flare location is important for determining the geo-effectiveness of flare-associated particle and CME events.

The X-ray monitor on GOES that is used to determine flare occurrence and GOES class is an irradiance monitor and, thus, has no knowledge of where the flare happened. As a result, the EVE flare catalog uses five different sources to determine the average location of a flare. The first two are from NOAA: the optical flare location and the active region location. The optical flare location is derived from the NOAA Solar Event reports and is determined in the NOAA Events module (Section 4.3). The active region location is derived from the Solar Region Summary reports and is determined in the Active Region module (Section 4.4). Flare-active region association is determined by SWPC operator and included in the SGAS report. The majority of flares occur in active regions but because active regions can be quite large, the active region location is generally the least reliable method to obtain the flare location. The next two flare location methods use EVE data directly: ESP quad-diode ratios and SAM soft X-ray images. The latest location comes from the Heliophysics Event Knowledge database (HEK), which includes the results of several flare finder algorithms using AIA images. The last three methods will be discussed in detail in the following sections. These locations as well as some of the data used in calculating locations from EVE data are stored in the LOCATION IDL structure (Table 4.10).

Table 4.10: Description of the LOCATION IDL structure

Tag Name	Type	Description
flare_id	String	Flare ID
pbOr	Double array	P-angle, $B_0$ -angle, and apparent solar radius for calculating locations.
l0	Double	Longitude of central meridian.
avg_location	String	Average flare location.
avg_longitude	Float	Average longitude.
avg_latitude	Float	Average latitude.
noaa_location	String	NOAA flare location.
noaa_longitude	Float	NOAA longitude.
noaa_latitude	Float	NOAA latitude.
ar_location	String	Active region location.
ar_longitude	Float	Active region longitude.
ar_latitude	Float	Active region latitude.
esp_preflare_quad	Float array	Pre-flare ESP quadrant diode irradiance values used for calculating flare location from ESP.
esp_flare_quad	Float array	Flare ESP quadrant diode irradiance values used for calculating flare location from ESP.
esp_x	Float	ESP normalized x-position.
esp_y	Float	ESP normalized y-position.
esp_location	String	ESP flare location.
esp_longitude	Float	ESP longitude.
esp_latitude	Float	ESP latitude.
sam_x	Float	SAM pixel location.
sam_y	Float	SAM pixel location.
sam_alpha	Float	SAM plane-of-sky angle.
sam_beta	Float	SAM plane-of-sky angle.
sam_location	String	SAM flare location.
sam_longitude	Float	SAM longitude.
sam_latitude	Float	SAM latitude.
hek_location	String	Flare location using HEK Method 1
hek_longitude	Float	Longitude from HEK Method 1.
hek_latitude	Float	Latitude from HEK Method 1.
hek2_location	String	Flare location using HEK Method 2
hek2_longitude	Float	Longitude from HEK Method 2.
hek2_latitude	Float	Latitude from HEK Method 2.

#### 4.5.1 ESP Quad-diode Location

ESP, part of the EVE instrument suite, measures the soft X-ray flux from 0.1–7.0 nm using a quadrant diode or “quad-diode”. A quad-diode is a diode where each quadrant is read out independently. The total of the four quadrants provides the irradiance measurement while the ratio of the quadrants provides the “center-of-brightness” location on the plane of the sky. A quad-diode does not image the Sun. Instead, it

measures the angle of the Sun or flare relative to the boresight of the instrument.

In one dimension, assuming a uniform source, the signal on each half of the diode is proportional to the illuminated portion of the diode (Figure 4.4) and related to the angle between the Sun and boresight of the aperture,  $\theta$  by

$$\frac{E_L}{E_L + E_R} = \frac{\left(\frac{W}{2} - L \tan \theta\right)}{W} \quad (4.2)$$

$$\frac{E_R}{E_L + E_R} = \frac{\left(\frac{W}{2} + L \tan \theta\right)}{W} \quad (4.3)$$

where  $W$  is the aperture width,  $L$  is the distance between the aperture and diode,  $E_L$  and  $E_R$  are the signal on the left and right diodes respectively. Combining Equations 4.2 and 4.3 and solving for the angle yields:

$$\tan \theta = \left(\frac{W}{2L}\right) \left(\frac{E_L - E_R}{E_L + E_R}\right) \quad (4.4)$$

The flare location using ESP is done in two dimensions using all four quadrants. First, the pre-flare irradiance for each quadrant is subtracted from the peak irradiance so that the center-of-brightness of the Sun is removed to generate  $E_1, E_2, E_3, E_4$ . Next, normalized coordinates ( $x$  and  $y$ ) are calculated using:

$$x = \frac{(E_1 + E_2) - (E_3 + E_4)}{E_1 + E_2 + E_3 + E_4} \quad (4.5)$$

$$y = \frac{(E_1 + E_3) - (E_2 + E_4)}{E_1 + E_2 + E_3 + E_4} \quad (4.6)$$

These normalized coordinates are then converted to angles in the plane of the sky:

$$\alpha = m_\alpha x + b_\alpha \quad (4.7)$$

$$\beta = m_\beta y + b_\beta \quad (4.8)$$

Here,  $\alpha$  is the angle in the East-West direction while  $\beta$  are the angle in the North-South direction. The coefficients ( $m_\alpha, b_\alpha, m_\beta, b_\beta$ ) are determined from the quarterly ESP field-of-view maps. Finally,  $\alpha$  and  $\beta$  are converted to heliographic latitude and longitude on the Sun using standard IDL routines.

#### 4.5.2 Brightest pixel location in SAM Images

SAM is a pinhole X-ray imager with the same filter as the ESP quad-diode. SAM images are recorded on a unused portion of the MEGS-A CCD and have a spatial resolution of 15 arc-seconds. While SAM

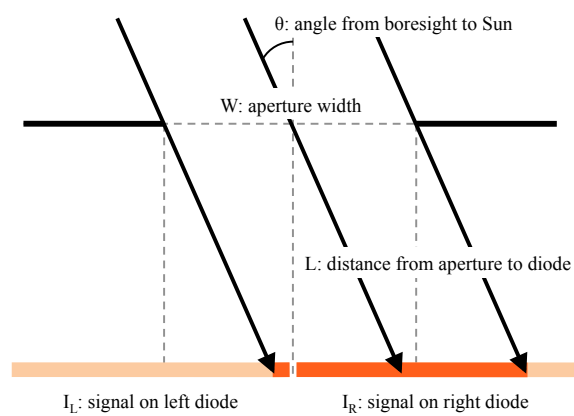


Figure 4.4: Schematic showing how center-of-brightness can be determined using a quad-diode like the ESP 0-7 nm channel. The signal on each half of the diode is proportional to the illuminated portion of the diode, which in turn is determined by the angle between the Sun and boresight as well as the aperture width, and distance from the aperture to the diode.

images could be produced every 10-seconds when the MEGS A CCD is readout to produce the MEGS spectra, multiple images are co-added to increase the effective integration time and the signal-to noise.

During a flare, the location of the flare becomes obvious. The SAM is designed to measure soft X-rays. During flares, however, it also measures hard X-rays. The short wavelength cutoff of SAM's bandpass is determined not by a filter but by the solar spectrum and detector efficiency. SAM's pinhole aperture is made of beryllium copper and is mounted to a tantalum shield. Soft X-rays are blocked by the beryllium copper and can only go through the small pinhole aperture. Hard X-rays, on the other hand, are blocked by the tantalum but can go through the beryllium copper. Normally, the Sun does not emit hard X-rays. During a flare, however, the Sun emits enough hard X-rays that the SAM tantalum shield acts as a second pinhole camera with a larger aperture. As seen in Figure 4.5, the location of the flare is readily apparent.

The location of the flare in a SAM image is determined by spatially smoothing the image and then finding the pixel with the most counts. This pixel location is then converted into heliographic coordinates. This is done for every 5-minute integration and recorded in the L0C SAM space weather product.

#### **4.5.3 Location in AIA Images from the HEK**

The location of a solar flare can also be determined from AIA images. Flare locations determined by finding the pixels that suddenly increase in brightness are recorded in the Heliophysics Event Knowledgebase (HEK, Hurlburt et al. 2012). Currently, there are two flare detection algorithms in the HEK. The first is included in the Solarsoft distribution while the second was developed by the AIA feature finder team (Martens et al. 2012). Both of these algorithms work by first heavily binning AIA images (the feature finder algorithm uses  $16 \times 16$  macropixels) and then applying a peak detection algorithm to the integrated signal in each macropixel. Once a flare is found, the higher spatial resolution images are used to determine flare time and location.

These flare detection algorithms run automatically on AIA images and flare time and location are submitted to the HEK. By querying the HEK through Solarsoft via `ssw_her_make_query` and `ssw_her_query`, I am able to find all HEK flares that occur between the GOES start time and GOES end time of the flare. I then report the mean location of all the events for each of the flare detection algorithms.

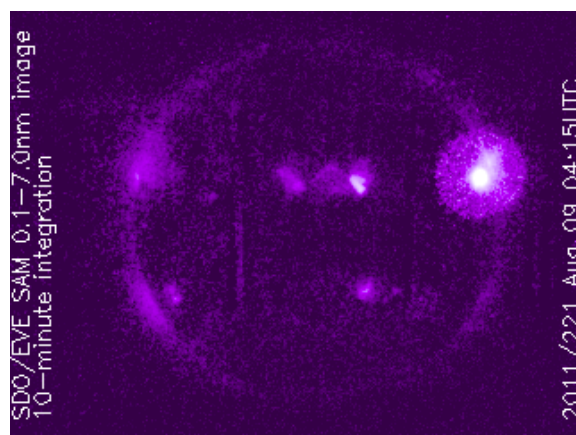


Figure 4.5: Image of the X6.9 flare on 9 August 2011 created using 10-minutes of integrations. The flare occurs near the northwest limb and is easily identifiable by the halo of hard X-rays.

#### 4.5.4 Comparison of Location Methods

While each of these flare location methods use different data, they all produce consistent results. Figure 4.6 shows a comparison of the different techniques.

For the HEK locations, the spread in latitude results from blooming in the AIA images. During solar flares, the AIA CCDs can saturate. This saturation can then spill over into neighboring pixels, an effect called “blooming”. The AIA CCDs bloom in the North-South direction. The AIA flare detection algorithms have a difficult time determining the latitude of the flare when partial column of saturated pixels.

Overall, these uncertainties are not that important for flare location. In general, the average location is good enough to find the flare in AIA images and determine whether the flare occurred over the limb. The geoeffectiveness of solar events is based on wide longitudinal regions.

Figure 4.7 shows the location of each flare in the EVE flare catalog from 1 May 2010 to 1 November 2011 with each panel covering a 6-month time period. The frequency and GOES class of flares has increased markedly since the beginning of the SDO mission. There is also an asymmetry in flare frequency between the Northern and Southern hemispheres.

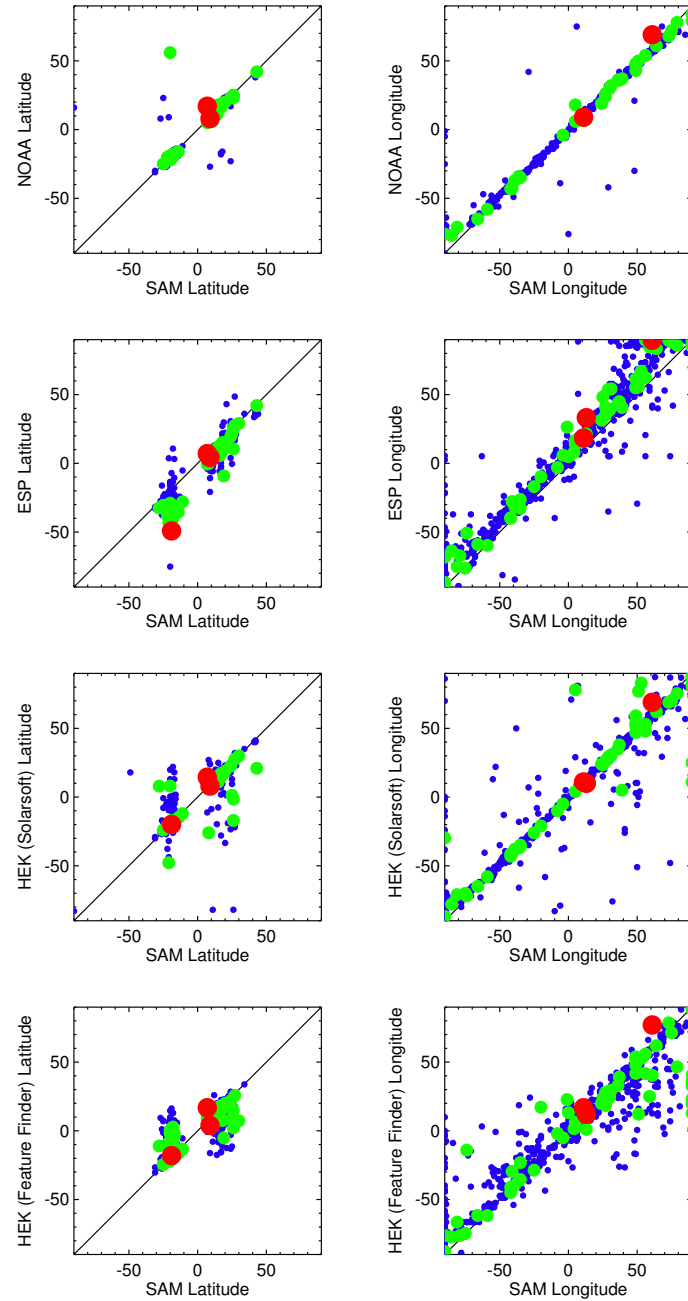


Figure 4.6: Comparison of flare location methods. The color and size of circles indicate the size of the flare (C-class is blue, M-class is green, and X-class is red).

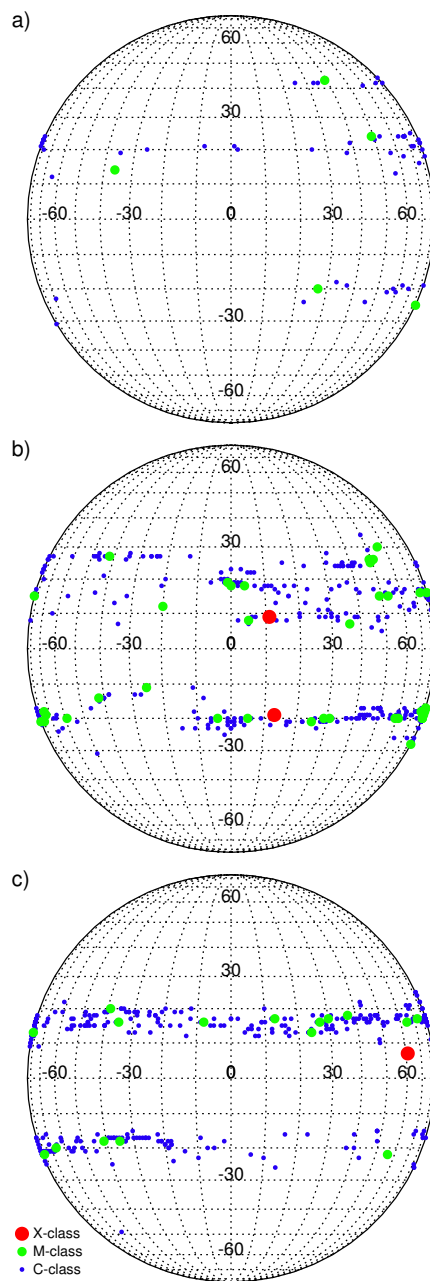


Figure 4.7: Location of flares in the EVE flare catalog for (a) 1 May 2010 to 31 October 2010, (b) 1 November 2010 to 31 March 2011, and (c) 1 April 2011 to 31 August 2011. The color and size of circles indicate the size of the flare (C-class is blue, M-class is green, and X-class is red).

## 4.6 CME Module: Associating Flares with Coronal Mass Ejections

The association between solar flares and coronal mass ejections (CMEs) is not fully understood. CMEs can occur without a solar flare and not all solar flares have a CME counterpart. Weak solar flares generally never have associated CMEs while strong flares almost always do. By including CME association in the EVE flare catalog, it is possible to explore why some flares have CMEs and others do not. The output of the CME module is stored in the CME IDL structure (Table 4.11).

Table 4.11: Description of the CME IDL structure

Tag Name	Type	Description
flare_id	String	Flare ID.
flare_location	String	Flare location used for matching to CMEs.
flare_longitude	Float	Flare longitude.
flare_latitude	Float	Flare latitude.
flare_start_time	String	Start time of the flare (UT).
flare_start_time_jd	Double	Julian date of the start time of the flare.
angle_lasco	Double	Position angle of flare as viewed from SOHO.
cme_lasco_cdaw	Structure	Best-match CME from CDAW catalog.
cme_lasco_cactus	Structure	Best-match CME from LASCO CACTUS catalog.
angle_secchi_a	Double	Position angle of flare as viewed from STEREO A.
cme_secchi_a	Structure	Best-match CME from SECCHI A CACTUS catalog.
angle_secchi_b	Double	Position angle of flare as viewed from STEREO B.
cme_secchi_b	Structure	Best-match CME from SECCHI B CACTUS catalog.

### 4.6.1 Coronagraphs

CMEs are observed in whitelight coronagraphs, which block the solar disk to observe the faint outer corona (Figure 4.9 shows an image from a coronagraph). Currently, there are three spacecraft with whitelight coronagraphs: SOHO, STEREO A, and STEREO B. SOHO orbits the Sun at the first Lagrangian point, between the Sun and the Earth. The STEREO spacecraft orbit the Sun slightly ahead (STEREO A) and behind (STEREO B) the Earth, causing the spacecraft to drift away from the Earth. During the first year of the SDO mission, the STEREO spacecraft reached 180° separation. Figure 4.8 shows the locations of SOHO, STEREO A and STEREO B relative to the Earth and the Sun.

The different view points of the three coronagraphs are important for studying flare-CME association.

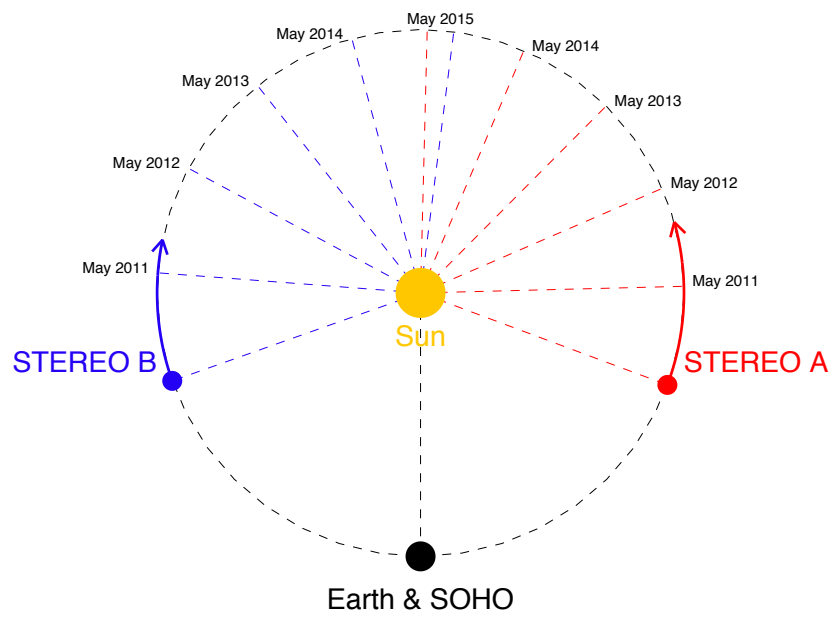


Figure 4.8: Location of the two STEREO spacecraft during the first 18 months (solid line) of the SDO Mission relative to the Earth and the SOHO spacecraft. The dashed lines indicate the location of the STEREO spacecraft every year on 1 May for the SDO primary mission.

Properties of CMEs are best determined when the CME is observed in the plane of the sky as this limits projection effects. For CMEs that originate at disk-center for SDO and SOHO, the STEREO coronagraphs can observe the CME in the plane of the sky. For CMEs closer to the limb for SDO, SOHO has the best viewing angle. Furthermore, CMEs are faint and can be difficult to detect. Having multiple coronagraphs with different viewing angles helps capture all CMEs.

By the end of the primary SDO mission, both STEREO spacecraft will be behind the Sun, making it difficult to detect and measure CMEs that originate at disk-center for SDO. Moreover, SOHO is an old spacecraft and may fail at anytime, which would further limit our ability to observe CMEs. This makes it important to understand the flare-CME relationship now when we have the three different coronagraphs and the observations from SDO.

#### 4.6.2 CME Catalogs

There are two different CME catalogs. The CDAW catalog is generated and maintained at the CDAW Data Center by NASA and The Catholic University of America in cooperation with the Naval Research Laboratory. The CDAW catalog is assembled by human operators using observations from SOHO. It is available as a single text file for the entire SOHO mission ([http://cdaw.gsfc.nasa.gov/CME\\_list/UNIVERSAL/text\\_ver/univ\\_all.txt](http://cdaw.gsfc.nasa.gov/CME_list/UNIVERSAL/text_ver/univ_all.txt)).

The CACTUS catalog autonomously detects coronal mass ejections (CMEs) in image sequences from SOHO or STEREO and was developed at the Royal Observatory of Belgium (Robbrecht & Berghmans 2004). The LASCO CACTUS catalog is available from [http://sidc.oma.be/cactus/catalog/LASCO/2\\_5\\_0](http://sidc.oma.be/cactus/catalog/LASCO/2_5_0) while the STEREO CACTUS catalogs are available from <http://secchi.nrl.navy.mil/cactus/SECCHI-A/> and <http://secchi.nrl.navy.mil/cactus/SECCHI-B/>.

Both catalogs contain essentially the same information: date and time of first appearance of CME in coronagraph, position angle (PA), angular width in degrees, speed, and acceleration. The position angle is the central angle of the CME measured counterclockwise from solar north in the plane of the sky (Figure 4.9). Table 4.12 describes the CME parameters that are extracted from the CME catalogs and stored in the CME IDL structure.

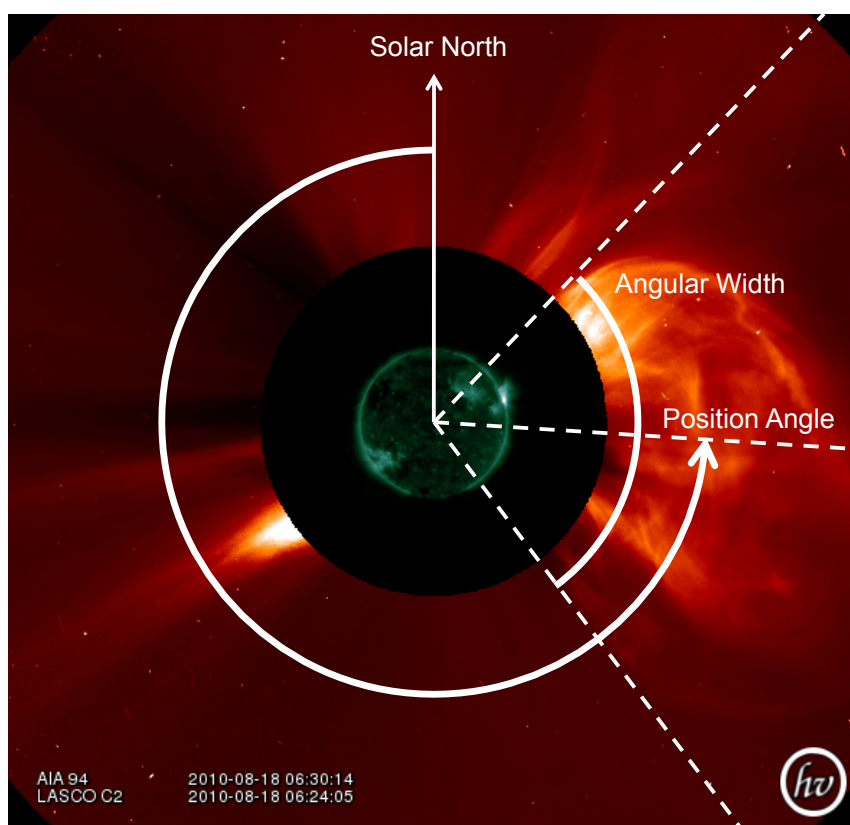


Figure 4.9: Example of a CME from SOHO showing how the position angle and angular width are defined. A simultaneous AIA image shown to scale shows the likely origin of the CME on the western limb of the Sun.

Table 4.12: Information extracted from the CME catalogs. The third and fourth columns indicate whether the CME parameter is included in each of the CME catalogs.

Tag Name	Type	CDAW	CACTUS	Description
instrument	String	✓	✓	Coronagraph (LASCO, SECCHI_A, or SECCHI_B).
catalog	String	✓	✓	CME Catalog (CDAW or CACTUS).
cme_id	String		✓	CME ID number used in CACTUS catalog to identify the CME.
date	String	✓	✓	Start time of CME
year	Integer	✓	✓	Year of CME start time
month	Integer	✓	✓	Month of CME start time
day	Integer	✓	✓	Day of CME start time
doy	Integer	✓	✓	Day of year for CME start time
sod	Long	✓	✓	Seconds of day for CME start time
jd	Double	✓	✓	Julian date of CME start time
duration	Integer		✓	Duration of CME in hours.
position_angle	Integer	✓	✓	CME position angle (degrees counter-clockwise from solar North).
angular_width	Integer	✓	✓	Angular width of CME (degrees)
velocity	Float	✓	✓	Plane-of-sky linear speed of CME ( $\text{km s}^{-1}$ )
sigma_velocity	Float		✓	Standard deviation of speed of CME ( $\text{km s}^{-1}$ )
min_velocity	Float		✓	Minimum of speed of CME ( $\text{km s}^{-1}$ )
max_velocity	Float		✓	Maximum of speed of CME ( $\text{km s}^{-1}$ )
speed_2nd_order_initial	Float	✓		Initial second order speed of CME ( $\text{km s}^{-1}$ )
speed_2nd_order_finial	Float	✓		Final second order speed of CME ( $\text{km s}^{-1}$ )
speed_2nd_order_20r	Float	✓		Second order speed of CME at $20 R_{\odot}$ ( $\text{km s}^{-1}$ )
acceleration	Float	✓		Acceleration of CME ( $\text{km s}^{-2}$ )
mass	Double	✓		Mass estimate of CME (kg)
kinetic_energy	Double	✓		Kinetic energy ( $Q_{KE} = \frac{1}{2}mv^2$ ) of CME (J)
mpa	Integer	✓		Measurement position angle
remark	String	✓		Operator comments

### 4.6.3 Matching Flares and CMEs

Presently, it is not possible to observe a flare and its associated CME in the field-of-view of the same instrument or in overlapping fields-of-view of different instruments. While AIA observes eruptions that can become CMEs, the limited AIA field-of-view makes it impossible to determine whether material actually escapes the corona and forms a CME. Associating a CME with a particular flare in an automated way is about making an educated guess. CMEs associated with flares should be temporally and spatially connected to the flare. Because this is a flare catalog, I use information about the flare to find the best matched CME in each of the CME catalogs. For a different use, it would be possible to use a list of CMEs to find the best matched flare.

There is two criteria for finding a flare-associated CME. First, a flare-associated CME must occur after the flare. CMEs are observed in coronagraphs which have an inner boundary at  $2 R_{\odot}$ . So while the CME may physically lift-off from the corona simultaneously with the formation of flare loops, the CME will be observed in the coronagraph after the flare is observed by GOES. The detailed analysis by Mahrous et al. (2009) shows that most CMEs are observed within two hours after the flare. To be generous and to ensure that I capture slow CMEs, I look for CMEs where the start time  $t_{CME}$  is within three hours of the GOES flare start time  $t_{flare}$ .

The second criteria, a flare-associated CME should originate in the same sector as the flare. While deflection of CMEs are possible (Mohamed et al. 2012), it is uncommon. To match CMEs and flares spatially, I determine the position angle of the flare as viewed from each spacecraft,  $\theta_{flare}$ . This is done in two steps. First, I convert the latitude  $\phi$  and longitude  $\lambda$  of the flare into x-, y- coordinates in the plane of the sky:

$$x = \cos(\phi) \sin(\lambda - L_0) \quad (4.9)$$

$$y = \sin(\phi) \cos(B_0) - \cos(\phi) \cos(\lambda - L_0) \sin(B_0) \quad (4.10)$$

Next, these are used to calculate the position angle for the flare,  $\theta_{flare}$ :

$$\theta_{flare} = 360^\circ - \tan^{-1} \left( \frac{x}{y} \right) \quad (4.11)$$

A CME is considered to associated with a given flare if both criteria are met:

$$t_{flare} < t_{CME} < t_{flare} + 3 \text{ hours} \quad (4.12)$$

$$\theta_{flare} - \left(15^\circ + \frac{w_{CME}}{2}\right) < \theta_{CME} < \theta_{flare} + \left(15^\circ + \frac{w_{CME}}{2}\right) \quad (4.13)$$

where  $\theta_{CME}$  is the position angle of the CME and  $w_{CME}$  is the angular width of the CME

## 4.7 EVE Module

### 4.7.1 EVL IDL Structure

The first part of the EVE module quantifies how the EUV irradiance changes during a solar flare. This module analyzes the light curve of every extracted line, band, and diode (See Tables 3.2, 3.4, and 3.5) in the EVE Level 2 EVL data product and stores the result in the EVL IDL structure (Table 4.13). The EVL data product is used because the extracted lines are some of these brightest lines observed by EVE and generally not blended with other lines. They also coverage a wide range of temperatures.

Table 4.13: Description of the EVL IDL structure

Tag Name	Type	Description
<code>flare_id</code>	String	Flare ID
<code>evl_lines</code>	Structure	Flare parameters for the Level 2 EVL lines defined in Table 3.4
<code>evl_diodes</code>	Structure	Flare parameters for the Level 2 EVL lines defined in Table 3.2
<code>evl_bands</code>	Structure	Flare parameters for the Level 2 EVL lines defined in Table 3.5

For each light curve in the extracted lines data product, several key quantities are determined. The goal is for these parameters to sufficiently describe the flare response in each EUV line. Table 4.14 lists the various parameters that extracted from each light curve.

The pre-flare irradiance is calculated by finding the mean of the irradiance during the pre-flare time interval discussed in Section 4.2:

$$E_{preflare} = \langle E(t_{preflare\_start\_time} : t_{preflare\_end\_time}) \rangle \quad (4.14)$$

Table 4.14: Description of the EVL flare parameters.

Tag Name	Type	Description
evl_tag	String	Line/band/diode tag name in Level 2 EVL structure.
evl_label	String	Label for the line/band/diode. For EVL lines, this includes the ion, wavelength, and formation temperature.
preflare_irrad	Double	Pre-flare or background irradiance in $\text{W m}^{-2}$ .
peak_irrad	Double	Peak flare irradiance in $\text{W m}^{-2}$ .
peak_time	String	Peak time of the flare (UT).
peak_time_jd	Double	Julian date of the start time of the flare.
rise_25_time	String	Time during the rising phase when the irradiance is 25% of peak value (UT).
rise_25_time_jd	Double	Julian date of the time during the rising phase when the irradiance is 25% of peak value.
rise_50_time	String	Time during the rising phase when the irradiance is 50% of peak value (UT).
rise_50_time_jd	Double	Julian date of the time during the rising phase when the irradiance is 50% of peak value.
rise_75_time	String	Time during the rising phase when the irradiance is 75% of peak value (UT).
rise_75_time_jd	Double	Julian date of the time during the rising phase when the irradiance is 75% of peak value.
decay_25_time	String	Time during the decay phase when the irradiance is 25% of peak value (UT).
decay_25_time_jd	Double	Julian date of the time during the decay phase when the irradiance is 25% of peak value.
decay_50_time	String	Time during the decay phase when the irradiance is 50% of peak value (UT).
decay_50_time_jd	Double	Julian date of the time during the decay phase when the irradiance is 50% of peak value.
decay_75_time	String	Time during the decay phase when the irradiance is 75% of peak value (UT).
decay_75_time_jd	Double	Julian date of the time during the decay phase when the irradiance is 75% of peak value.
energy_25	Double	Integrated irradiance between 25% rise and decay times in $\text{J m}^{-2}$ .
energy_50	Double	Integrated irradiance between 50% rise and decay times in $\text{J m}^{-2}$ .
energy_75	Double	Integrated irradiance between 75% rise and decay times in $\text{J m}^{-2}$ .

This pre-flare irradiance can be subtracted from peak flare irradiance to isolate the contributions to the EUV irradiance from the flare. The pre-flare irradiance is also used to calculate the flare energy (time-integrated irradiance).

The most obvious parameter to measure is the peak flare irradiance. To find the peak in the irradiance

light curve associated with the flare is done in several steps. I first determine the time range to search for the peak. The flare peak, even for lines dominated by the impulsive phase, cannot occur prior to the start time of the flare. The peak should also occur before the next flare starts. In the event that the next flare is days later, the code stops looking for a peak 24 hours after the flare start time.

After I have determined the window to search for the flare peak, I locate the peak. Mathematically, the local maximum occurs where the time derivative of the irradiance goes from being positive to being negative.

First, to reduce noise the time series is heavily smoothed by 60 integrations (10 minutes). Any missing data is also filled in. The smoothing eliminates small peaks, making it easier to find the peak associated with the flare. Then the time derivative is calculated using the IDL function `deriv`. Next, the code looks for the first occurrence of where the time derivative is positive for 15 integrations (2.5 minutes) and the first occurrence after that where the slope is negative for 6 integrations (1 minute). These set a time range for when the peak occurs. Using the unsmoothed data, the maximum in irradiance between these two times is found. This gives the peak time and irradiance,  $E_{flare}$ .

The time of the peak is just as important as the peak irradiance. During a flare, the enhancements in the EUV are a result of the flare loops radiatively cooling. We expect cooler lines to peak after hotter lines. By comparing the measured delay with what is expected theoretically, the heating and radiative cooling of flare loops can be studied.

Flare duration is another important parameter. Duration is the rise time plus the decay time. Usually, the 50% level is used to calculate rise and decay times. For completeness and to test whether the 50% level is the best, the rise and decay times determined at 25%, 50%, and 75% levels are calculated. To find the rise and decay times, the code looks for when the EUV irradiance crosses a threshold during the rise of the flare and during the decay (Figure 4.10). The irradiance levels used for determining the rise and decay times are

found using:

$$E_{25\%} = 0.25 (E_{flare} - E_{preflare}) + E_{preflare} \quad (4.15)$$

$$E_{50\%} = 0.50 (E_{flare} - E_{preflare}) + E_{preflare} \quad (4.16)$$

$$E_{75\%} = 0.75 (E_{flare} - E_{preflare}) + E_{preflare} \quad (4.17)$$

The final set of flare parameters is the energy. The energy is defined as:

$$Q = \int_{t_{rise}}^{t_{decay}} (E(t) - E_{preflare}) dt \quad (4.18)$$

and is calculated for the 25%, 50%, and 75% levels.

#### 4.7.2 EVE Plots

The second part of the EVE module produces two sets of plots to visualize the EVE data. The first set of plots is a multiple page PDF with the light curves for every extracted line, band, and diode analyzed in the EVL IDL structure. The EVL lines are sorted by temperature rather than wavelength.

The second set is a one-page PDF containing the quicklook plots (Figure 4.11). This multi-panel page includes the GOES SXR light curves as well as key EVE lines such as the ESP 0-7 nm, the iron sequence (Fe IX to Fe XX) and He II 30.4 nm (measured both by MEGS and ESP). The lines are sorted by temperature with the hottest lines at the top (left column) and the coolest at the bottom (middle column). These quicklook plots are used for adding comments to the flare catalog via the IDL widget (see Section 4.9). In the iron sequence, radiative cooling the flare loops can be observed generally from Fe XX through Fe XV while coronal dimming can be seen in Fe IX and sometimes up to Fe XIV. While the ESP 30.4 nm diode has higher signal to noise compared to the MEGS 30.4 nm extracted line, the ESP diode contains emission from hotter lines as well.

The right column of the quicklook PDF contains a set of plots to examine the Neupert effect. By looking only at the rising phase of the flare, we can see the details of the impulsive phase. This column shows the GOES SXR, time-derivative as well as He II 30.4 nm (from MEGS) and RHESSI quicklook light curves. The RHESSI quicklook light curves are obtained through Solarsoft using `hsi_obs_summary`. These

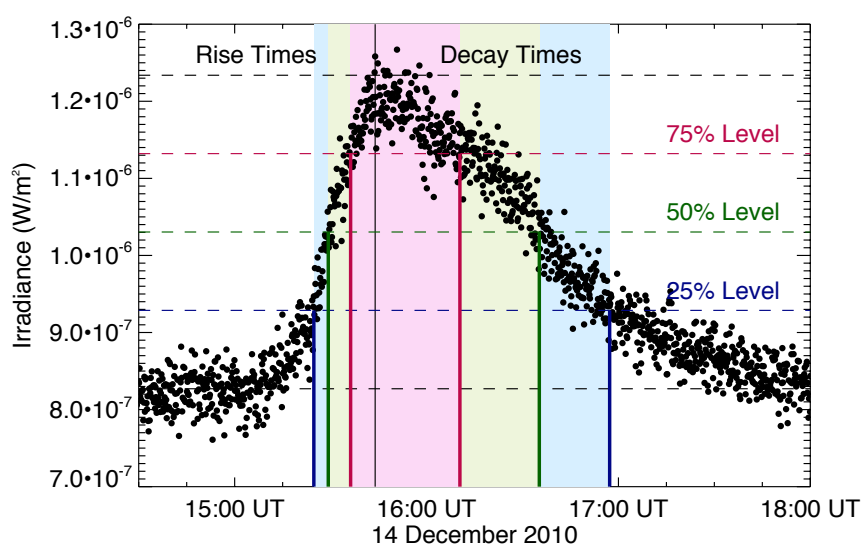


Figure 4.10: Example of how flare duration and energy are calculated for the Fe xx 13.3 nm line. The dashed horizontal lines indicate (from bottom to top) the pre-flare irradiance, the 25% (blue) level, the 50% (green) level, the 75% (pink) level, and the peak flare irradiance. The colored vertical lines indicate the rise (left) and decay (right) times for the 25%, 50%, 75% levels. The shaded regions indicate the timer range use to calculate flare energy for the 25%, 50%, 75% levels.

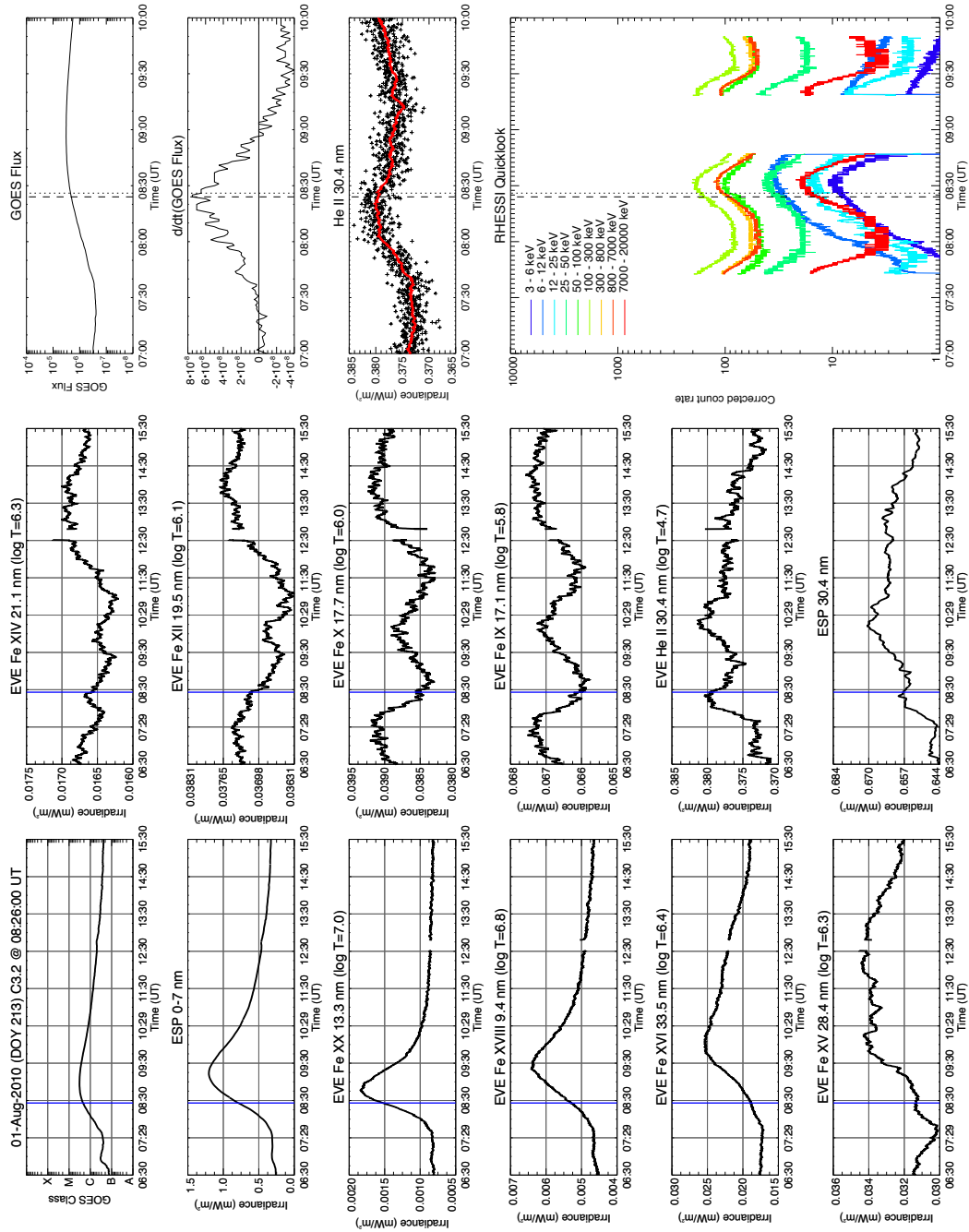


Figure 4.11: Example of the EVE quicklook plots for the C3.2 flare on 1 August 2010. The first two columns highlight the time evolution of the flare over nine hours. The vertical blue line marks the GOES peak time. The third column shows the Neupert effect with the dotted line showing the peak in the GOES SXR and the dashed line the peak in the time derivative of the SXR.

are quicklook data so no corrections have been applied. Generally, it is still fairly obvious whether there are hard X-rays ( $> 10$  keV) during the impulsive phase.

#### 4.8 AIA-EVE Movie Module

Using AIA images and EVE light curves, the AIA-EVE movie module generates a multi-panel MPEG movie. Figure 4.12 shows a frame from the AIA-EVE movie for the C3.2 movie on 1 August 2010. This movie uses the AIA synoptic images series, in which the full-resolution images are rescaled to 1024 by 1024 pixels and the time sampling is reduced to 2 minutes. This spatial and temporal resolution is sufficient for purposes of the flare catalog although for detailed analysis of an individual flare, the full resolution images should be used. The AIA synoptic images are available on-line from <http://jsoc.stanford.edu/data/aia/synoptic/>.

At the top of the movie (labeled 1 in Figure 4.12) is the flare ID and the time of the frame. Full-disk AIA 171 (labeled 2) and running difference images (labeled 3) provided an overview of the Sun during the flare. The difference images help highlight small flares, eruptions, and global features such as EIT waves (see Figure 4.13).

The white square in the AIA 171 image denotes the cutout region for the other AIA channels. This region is large enough ( $256 \times 256$  pixels or one-sixteenth of the full-disk image) to cover most active regions and is centered on the average flare location determined in the flare location module. These cutouts tracked the flaring region as it rotates. The four AIA channels used for the cutouts are AIA 131 (labeled 4 in Figure 4.12), AIA 335 (labeled 5), AIA 193 (labeled 6), and AIA 304 (labeled 7). These channels cover a range of temperatures. The AIA 131 channel observes hot flare emission and is closest to the soft X-ray while AIA 335 images warm coronal plasma. AIA 193 observes cool coronal plasma and, like AIA 171, shows both the flare loops, and coronal dimming. AIA 304 images the cooler transition region plasma which highlights the footpoints of the flare.

On the right side of the AIA-EVE movie are irradiance light curves. The top light curve (labeled 8) is the GOES SXR followed by Fe XX 13.3 nm, Fe XVI 33.5 nm, Fe IX 17.1 nm, and He II 30.4 (labeled 9-12) from MEGS. These emission lines cover the range of behavior observed in EVE as well as correspond to the dominant lines in the AIA channels. The dashed vertical line indicates the GOES peak time of the flare while the solid vertical line indicates the time of movie frame.

The AIA-EVE movie begins 30 minutes prior to GOES flare start time. The movie covers at least

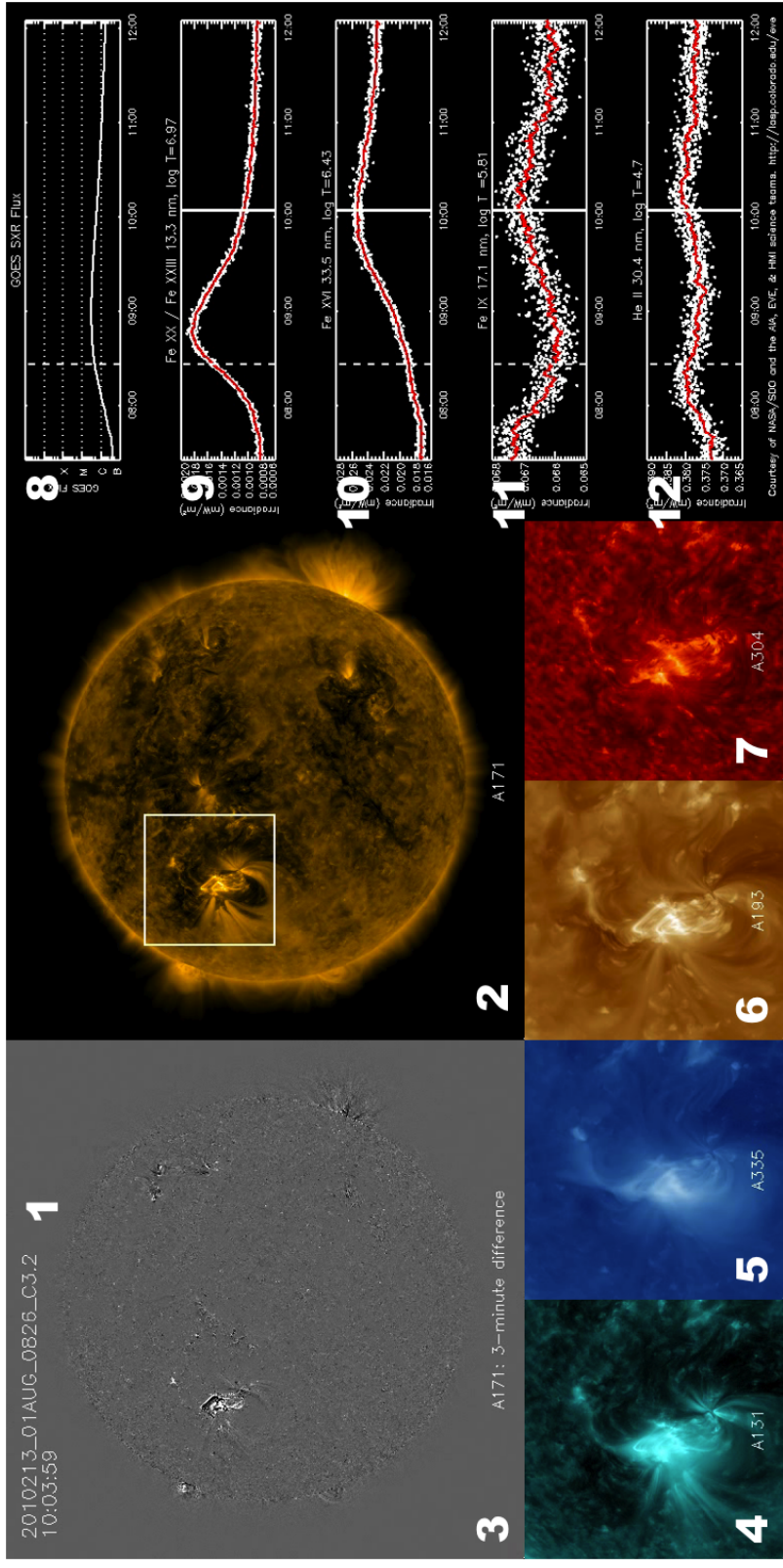


Figure 4.12: Example of a frame from the AIA-EVE movie for the C3.2 movie on 1 August 2010. The different panels are numbered and described in the text.

four hours. For long duration flares, the time coverage of the movie is expanded to 30 minute plus 2.5 times the duration of the flare defined by GOES. If a flare has a GOES start time of 14:00 UT and an GOES end time of 14:30 UT, the AIA-EVE movie covers 13:30 UT to 17:30 UT. If the same flare ended at 16:00 UT, the movie would cover 5.5 hours from 13:30 UT to 20:00 UT.

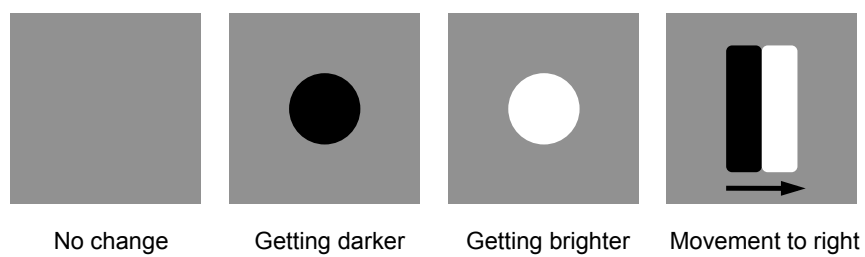


Figure 4.13: Understanding difference images. Difference images are grey where there is no change between the two images. Where a feature is getting dimmer, the difference image is black; where it is getting brighter, the difference image is white. A black region next to a white region shows the apparent movement of a feature. If the feature is bright, the movement is from the black region to the white region; if the feature is dark, the opposite holds true.